UNIVERSITY of CALIFORNIA
SANTA CRUZ

SPUTTERING ATOMIC LAYER AUGMENTED DEPOSITION: A NEW DEMONSTRATION OF ALUMINUM OXIDE–COPPER DIELECTRIC–METAL NANOCOMPOSITE THIN FILMS

A thesis submitted in partial satisfaction of the
requirements for the degree of

MASTERS OF SCIENCE

in

ELECTRICAL AND COMPUTER ENGINEERING

by

Jacob Sands

March 2022

The Thesis of Jacob Sands is
approved:

_____

Professor Nobuhiko Kobayashi

_____

Professor Marco Rolandi

_____

Professor Ali Yanik

_____

Peter Biehl
Vice Provost and Dean of Graduate Studies

Contents

List of Tables

List of Figures

Abstract

Sputtering Atomic Layer Augmented Deposition: A New Demonstration of Aluminum Oxide–Copper Dielectric–Metal Nanocomposite Thin Films

by

Jacob Sands

The specific machining process by which a thin film recipe is carried out determines the structure of each layer. For this reason, most precision thin films are coated using techniques involving chemical species because of their consistent ability to form uniform structures. However, the set of chemicals that is able to form thin films is more limited than the set of its cousin's technique of physically vaporizing a material source. Coupling this premise with the fact that it is advantageous to not expose a deposited sample to the atmosphere when transitioning from one deposition method to another, we were inspired to combine atomic layer deposition (ALD) and magnetron sputtering (SPU) within a single chamber– sputtering atomic layer augmented deposition (SALAD). By hybridizing the two techniques, SALAD is capable of both ALD's precise delivery and SPU's diversity of the materials. To demonstrate SALAD's structural and optical capabilities, we made seven different nanocomposites with 300 layers of aluminum oxide (AlO_x) and copper (Cu) thin films. After confirming that each AlO_x-Cu nanocomposite developed distinct layers without cross-contamination, we were surprised to see that the classical theory of effective medium approximation used to describe metal-dielectric optical properties did not apply to the measured spectroscopic reflectivity data.

Acknowledgements

I would like to thank my thesis advisor, Nobuhiko Kobayashi, for the opportunity to conduct this research. I would also like to thank Brian Giraldo and David Fryauf for their immense help establishing the groundwork for which the content of this paper is founded on. This project was partially supported by an NSF grant sponsored by Thomas Kuech and Kershed Cooper. The text of this thesis includes reprints of the following published material: *Demonstration of Sputtering Atomic Layer Augmented Deposition Aluminum Oxide–Copper Dielectric Dielectric–Metal Nanocomposite Thin Films*.

1

Introduction

This thesis investigates a new method of thin film growth called Sputtering Atomic Layer Augmented Deposition (SALAD). In particular, we reviewed the structural and optical properties of an interchanging copper and aluminum oxide thin film. Throughout the introductory chapter, I contextualize SALAD: how it came to be and where it might be going. I emphasize that there is a great diversity of potential applications and many unknowns, which likely implies that the technology may prove useful fodder for uncovering future novel phenomena. I further characterize the end of this chapter by outlining the rest of this thesis.

1.1 What is SALAD?

The crux of this project's idea arose when our lab attempted to develop a high-performance mirror from thermally evaporated silver (Ag) for the Thirty Meter Telescope. We found that by depositing aluminum oxide (AlO_x) by atomic layer deposition (ALD) and not physical vapor deposition (PVD) to create a protective

coating we could improve the robustness of the mirror's structure (Fryauf et al., 2015). This discovery led our lab to blueprint a new deposition apparatus that would be capable of optimizing thin film samples made for ground-based Ag telescope mirrors.

One of the main goals we sought in this new machine was to eliminate atmospheric exposure when a sample transitions from PVD to ALD or vice versa. By not breaking the vacuum to transition a slide from one machine of a particular deposition method to another, the sample would retain a higher purity since it would avoid atmospheric contaminants before the protective coating is applied. To satisfy this criterion, we could have used a system that deposits both Ag and AlO_x with ALD. However, the engineering required to do so would have been too convoluted or demanding to accommodate silver; so to develop the conditions for an ideal purity level that maintains a simple design, we sought to construct a system that combines both PVD and ALD in the same vacuum chamber, hence the resulting moniker of sputtering atomic layer augmented deposition.

1.2 What is SPU?

Sputtering (SPU) in the modern sense, with a parallel plate, is a thin film engineering staple that was first patented in the early 1960s. There have been many different variations of sputtering since then, but the general principle has not been compromised by the following half-century of innovation (Greene 2017). At its core, it is still considered to be the use of concentrated plasma-induced physical interactions

that erode individual or chunks of atoms of a desired material to coat a substrate with the resulting debris.

More specifically, the essence of the sputtering architecture can be broken down into three sections: (1) the parallel plates, (2) the chamber dimensions, and (3) the plasma. Some source material (more commonly known as the target) is placed on one plate connected to a cathode and the substrate is placed on the other plate, which is connected to an anode. The dimensions are designed after taking into account the theoretical minimum distance from target to substrate needed to maintain uniformity of the resulting layer. A minimum distance that configures the mean free path of the neutral atoms that are ejected from the target to be larger than the space in between the plates minimizes the potential for particle collisions in the vacuum chamber, for if the mean free path of the ejected target material is smaller than the space in between the plates, then they will scatter and distort the uniformity of the deposited thin film.

Furthermore, the chamber must be of a low enough pressure to not only minimize the scattering in the chamber but to ignite the plasma. Ignition occurs within the chamber by first accelerating the free electrons away from the cathode by enabling the voltage source. We used magnetron sputtering for the SALAD apparatus, so the magnetron-generated magnetic field that is located at the surface of the target catches most of the free electrons. Even though these electrons are concentrated in the magnetron field, they are still given energy by the cathode, so when a neutral gas atom is introduced to the chamber, like argon, a trapped electron has enough

energy during a collision to drive out an electron in the outer shell of the neutral gas particle, leaving it electrically unbalanced.

At this point, the newly generated positive ion is accelerated by the cathode, striking the target surface and blasting loose electrode material. Shrapnel from the target is then collected by the substrate like a plate underneath a dining table collecting crumbs. Conveniently, the act of generating atomic debris adds more free electrons to the chamber, which then feeds the continuation of plasma because the newly ejected electrons recombine with the generated positive ions. This continual stage of plasma bombardment that wears away the target is sputtering, so the thickness of an SPU film will be dictated by however long the thin film designer cares to allow the plasma to run ejected material onto the target (Greene 2017).

1.3 What is ALD?

Even though the use of the ALD method for thin film manufacturing had a lull before it became commercially important in the early 2000s, the history of atomic layer deposition is surprisingly similar to SPU. The seeming trend for most technology is to either be upgraded or replaced as the years go by, but both SPU and ALD are relatively simple techniques with a purpose that has not fundamentally changed since they were invented in the early 1960s (Parsons et al., 2013). That being said, the physical process of creating a thin film with SPU follows a different form because ALD falls into the umbrella category of chemical vapor deposition (CVD), meaning the film is generated via the substrate surface chemically reacting

with precursor materials.

An ALD growth can be boiled down to a few simple steps of pumping and purging. To use an example of how this is done, take the ALD process of depositing TiO_2 on a substrate. The ingredients needed for this specific recipe are two precursors, $TiCl_4$ and H_2O, and some neutral carrier gas like N_2. ALD's first step begins when $TiCl_4$ fills the empty chamber and reacts to the native hydroxyl groups on the substrate, forming a thin layer of $TiCl_3$. As a result, HCl is produced as a byproduct of the reaction that occurred on the substrate; therefore, along with the excess $TiCl_4$, the second step floods the chamber with a carrier gas N_2 to purge the particles that have not reacted to the substrate. The flow of carrier gas is then cut and summarily purged as well; so the third step, which occurs when no other gas is present in the chamber, pumps in the second precursor H_2O to react with the $TiCl_3$ layer. This reaction replaces chlorine with oxygen to form the desired TiO_2 layer. The fourth and final step is another N_2 purge sequence that rids the system of the newly developed HCl byproduct and the excess H_2O.

Additionally, the water in the chamber during the third step forms a new hydroxyl layer on top of the layer of TiO_2; so after the gaseous contents in the chamber are purged in the fourth step, the process may repeat back to step one if more layers of TiO_2 are desired. Here the specialty of ALD is apparent because an individual layer is constructed through a self-limiting reaction that restricts the growth of TiO_2 on locations that might break the uniformity. Whereas an SPU film thickness increases along with an increasing time interval of target-plasma exposure, ALD

growth is predicated by the number of monolayer sequences (Parsons et al., 2013).

1.4 Characteristics of SALAD

In the history of technological development, the engagement with the fringes of distinct disciplines in research has continuously generated new and unpredictable discoveries (e.g., magnetism and superconductivity). Patterns like these inspire hope in a simple machine that synthesizes two conventional techniques like SPU and ALD because the resulting thin films grown under such an apparatus may reside in a new form of physical phenomena that may be hidden by current unknowns. We feel especially confident that this may be a distinct possibility because SPU and ALD each have dichotomous shortcomings that limit their usability, which hopefully may be mitigated by the effect of SALAD's symbiotic design.

For instance, the physical nature of SPU prevents the highly controlled delivery of target material to the substrate, leading to clusters and vacancies that make SPU thin film analysis more difficult than layers made with CVD (Greene 20 17). ALD may be able to pick up the slack in this regard because it is capable of more accurate and precise control of thin film growth without the potential for inconsistent structural problems (Parsons et al., 2013). On the flip side, SPU has access to a wider variety of material elements because it is not limited like ALD to precursor reactions. For example, earlier it was mentioned that ALD deposited Ag requires a complex system to create quality layers, but this is a common issue for many other materials like niobium, copper, and platinum, which in turn means their thin films

are primarily deposited via PVD (Li & Gordon 2006; Kalutarage et al., 2014; Guo et al., 2015). Therefore, any technology that requires a material that is difficult or impossible to grow with ALD but not PVD may be streamlined under a SALAD system that hybridizes both techniques within the same chamber.

Shortcomings like these are more noticeable when a thin film requires a tight thickness control in the range of 0.1 nm (Elliot et al., 2014); so in our inaugural experiment of SALAD, we attempted to elucidate the potential corrective features that may arise from deposition synthesis via a chamber that is capable of operative procedures not found in conventional stand-alone SPU or ALD. These features may be sequential processes or quasi-concurrent depositions that are unattainable in cluster tools. Films resulting from either form of underrepresented logic of deposition operation may yield results that could be classified under a new subsection in thin film engineering– an untapped frontier for future research.

1.5 Further Applications of SALAD

Beyond the improvement of potential chemical shortcomings, we figured that it would also be advantageous to have a machine that could expedite the growth of interchanging layers of alternating deposition methods. To do this, designers usually use cluster systems, i.e. have SPU in one chamber, deposit, repressurize to match the common chamber, transition to the common buffer chamber, equalize the pressure to match the ALD chamber, transition to the ALD chamber, and then deposit the ALD layer, etc (Rossnagel, 2001). This method may serve the needs of the ma-

jority of current optical and electrical thin film research, but what if the desire is to have a large number of interchanging layers? Then one would need an almost inhumane motivation to repeat these steps for say one thousand layers. A machine that can automatically transition from SPU to ALD while maintaining reliable vacuum pressure would immensely accelerate the interchanging deposition cycle.

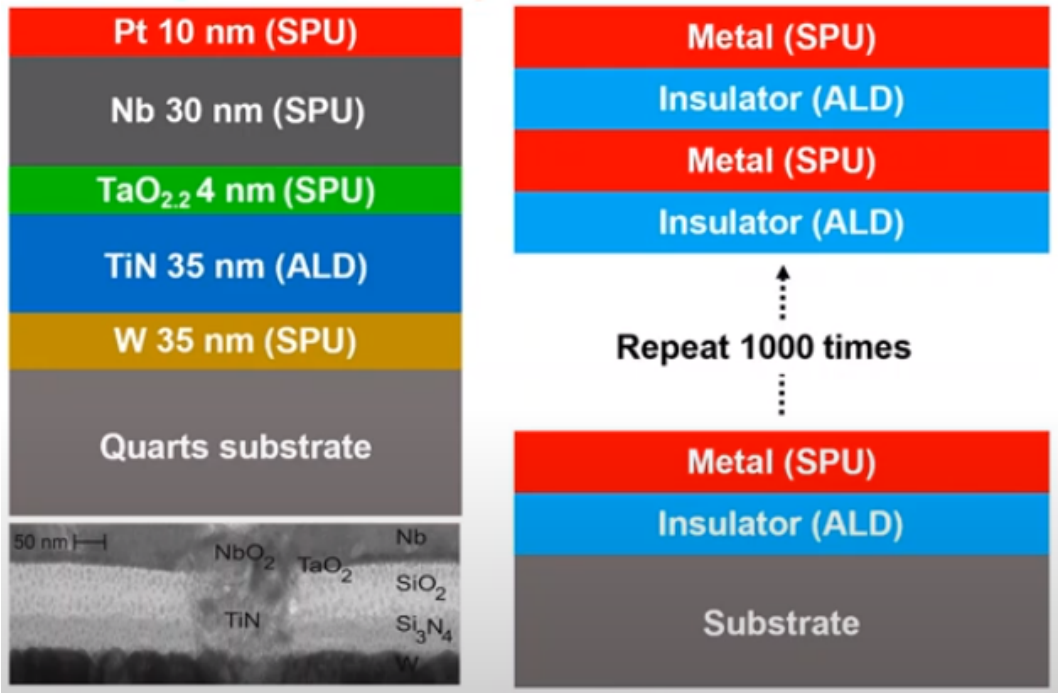

Figure 1.1: On the left is the architecture for a memristor on a quartz substrate. A system capable of depositing both ALD and SPU in the same vacuum could speedily churn out samples of such an architecture without difficulty. On the right is an example of what 1000+ interchanging layers of SPU and ALD would look like on a substrate. SALAD has the ability to accomplish such a task in record time with relative ease (Sands et al., 2020).

Another potential application has to do with certain restrictions that come about from designing technologies like resistive memory. As seen in Figure 1.1, SPU

was chosen to grow tantalum dioxide instead of ALD. Producing $TaO_{2.2}$ is not feasible with ALD, so a method of PVD must be present in the chamber to produce a non-stoichiometric thin film that is necessary for the multilayered memristor design (Parshina et al., 2021). Figure 1.2 models how to fine-tune these unique PVD compositions by sputtering more of the A material (α) and/or by sputtering more of the B material (β). Now, of course, a cluster system can grow the same chemical makeup, but the bulkiness of such a system appears overshadowed or outdated for commercial use when compared to the potential superior versatility of a fully functioning SALAD system.

Figure 1.2: A simple model designed to represent how sputtering creates non-stoichiometric thin films by depositing an (α) or (β) material on a stoichiometric layer. If more of material A is deposited, then the subscript 2 decrements per the material concentration represented by α. Similar logic is applied to material B but with an increment represented by β (Sands et al., 2020).

1.6 Our Method's Validity

Our objective in this experiment is to investigate the structural and optical properties of an AlO_x-Cu nanocomposite deposited under SALAD. Before doing this, we had to confirm that such a machine could be constructed, so we ran density modeling and computational fluid dynamics with finite element analysis to arrive at the structural parameters of the machine's design. Once blueprinted and built, we were able to deposit ALD and SPU on a substrate inside a commonly housed vacuum chamber. The combined information measured from X-ray spectroscopy and atomic force microscopy on the resulting SALAD sample provided sufficient chemical and surface information of the AlO_x-Cu nanocomposite to confirm that each layer is complete, consistent, and relatively pure in form. A thin film that is unable to meet these requirements would suggest that our newfound machine is not capable of growing thin films made of interchanging layers without cross-contamination.

An unpolarized light source combined with a monochrometer then captured the reflectance spectra of our nanocomposite samples. Effective variations between what was measured and what was modeled by the effective media approximation functioned as our primary inductive tool for optical analysis. Results from such a unique structure were somewhat expected to yield difficult to predict characteristics; however, the degree of variation between the classically approximated data and the measured data was nonetheless bewildering.

1.7 Outline of Thesis

In the rest of this thesis I expand on the methodology, results, and conclusions of the experiment. Specifically, in chapter two, I discuss the underpinnings for how we were able to arrive at the SALAD design. In chapter three, I explain how SALAD operates under a specific set of design parameters in order to deposit a thin film of interchanging AlO_x and Cu layers. For chapter four, I analyze our measured structural and optical results. Finally, in chapter five, I conclude by discussing the notable implications made by our research team in regards to the newfound information observed from SALAD's AlO_x-Cu nanocomposite sample.

2

Design of SALAD

In this chapter, I explain the design challenges of constructing a system that enables ALD and SPU to operate within the same vacuum chamber. I begin by labeling the initial design parameters and how we planned to enact a hybridized system via a fast-acting spatial divider. I discuss the data we collected through 2D computational fluid dynamics with finite-element analysis (CFD—FEA), the results of which determine the structural dimensions of what we believe to be an optimized environment. And, I conclude by updating the divider's design for real-world applications.

2.1 Initial Design Parameters

The preeminent design challenge was to find a way to isolate ALD and SPU from each other. Put another way, the goal was to deposit one pure layer of ALD material onto a substrate without cross-contamination from the sputtering gun. To do this, we came up with a spatial divider housed above the substrate and below the

sputtering gun. Figure 2.1 illustrates this more clearly in a cross-sectional view of the SALAD prototype design. As a whole, the system displays the main components: (1) SPU gun, (2) fast-acting spatial divider referred to as "divider", (3) ALD precursor inlet and outlet, and (4) substrate.

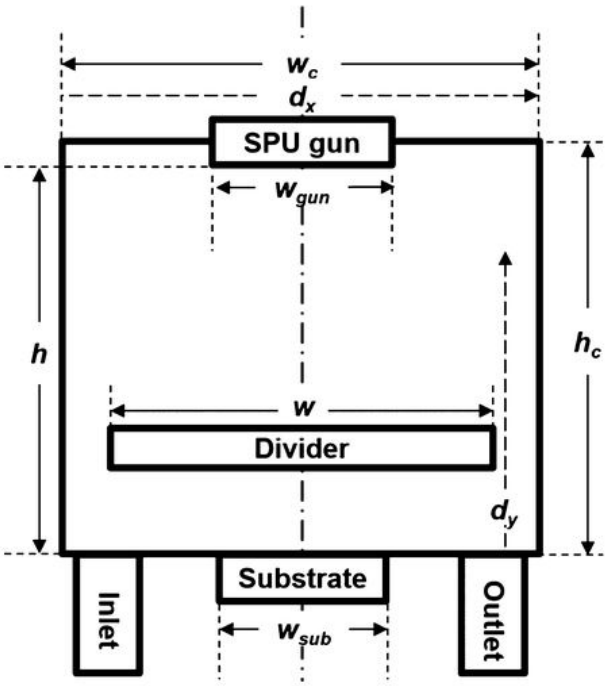

Figure 2.1: A prototype SALAD system used for the demonstration is schematically shown, revealing its details and basic concept. The system is equipped with an SPU gun on the cathode and "Divider". A substrate is placed underneath the divider. "Inlet" and "Outlet" direct carrier gases and precursors used in ALD. Several dimensional parameters used in the CFD–FEA are also denoted. (Giraldo et al., 2020)

In Figure 2.1, the dimension of the chamber height is labeled h_c and the diameter of the cylindrical chamber is labeled w_c. Dimensions of the divider were chosen for the piece to function as a block under both concurrent and sequential deposition modes while simultaneously being operable under a period of one second for its insertion and retraction steps. By running 2D CFD—FEA, we were able to config-

ure the width of the divider w in relation to w_c and the sputtering throw distance h that is needed to maximize the uniformity of the sputtered material. Table 2.1 summarizes the variables and fixed parameters of the dimensions and gas types for ALD and SPU used in the CFD—FEA (Giraldo et al., 2020).

Table 2.1: Key Parameters for Computational Fluid Dynamics with Finite Element Analysis

Parameter	Value
chamber width (w_c)	70 mm
chamber height (h_c)	h + 1 mm
throw distance (h)	$10-120$ mm (variable)
divider thickness	2 mm
divider width (w)	$10-90\%$ of w_c (variable)
divider location	70 mm
SPU gun width (w_{gun})	26 mm
substrate width (w_{sub})	20 mm
PVD gas type	argon at 300K
PVD pressure	1x10^{-3} Torr
ALD gas inlet and outlet width	5 mm
ALD gas type	argon at 300K
ALD inlet pressure	760 Torr
ALD mass flow	20 sccm
ALD outlet pressure	1x10^{-3} Torr

2.2 CFD—FEA of SPU

In order to optimize the deposition environment for ALD and SPU in the same vacuum, the divider that would insert and retract in the chamber must be housed in a way to permit the laminar flow needed for the ALD precursor to uniformly coat the substrate while maintaining the desired height for the SPU target to maximize a uniform throw radius. Figure 2.1 uses two orthogonal directions d_x and d_y to respectively represent the distance beginning at the left of the wall of the divider

and the point of location for the divider beginning at the location of the substrate. Or more precisely, if d_x = d_y = 30 mm, then the divider has a space of 30 mm from the left of the wall and it inserts and retracts 30 mm above the substrate. Additionally, the SPU gun width w_{gun} was chosen to be relatively small to ensure a more cost-efficient design that maintains a uniform spatial density of the sputtered species (ρ_{spu}).

Figure 2.2a,b shows a density gradient of ρ_{spu} for two different heights h, (a) 10 mm and (b) 80 mm. The results indicate that the increase of h significantly evens out the density distribution, which leads to the desired uniform distribution of sputtered material on the substrate at some level of h. Figure 2.2c finds the minimum distance to allow such a uniformity by graphing the nonuniformity as a function of h defined as such: ($\rho_{spu-max}$ - $\rho_{spu-min}$)/$\rho_{spu-min}$. Here, $\rho_{spu-max}$ and $\rho_{spu-min}$ represent the maximum and minimum sputtered densities found across the substrate. The graphical result informs us of the minimum sputtered throw distance needed to achieve uniformity on the substrate, by way of the initial point of the emergent plateau at 60 mm.

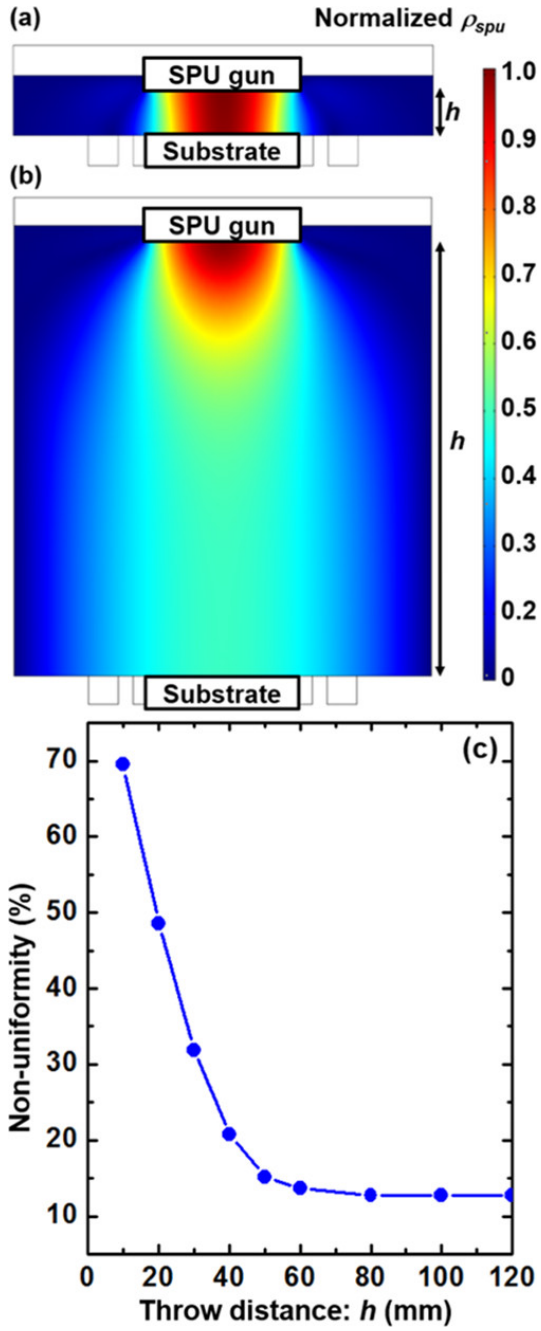

Figure 2.2: Distribution maps in (a) and (b) of normalized ρ_{spu} in the chamber with two different h, indicating the uniformity of ρ_{spu} improves as h increases. Nonuniformity in (c) of ρ_{spu} across the substrate is plotted as a function of h, indicating h needs to be at least 60 mm. (Giraldo et al., 2020)

2.3 CFD—FEA of ALD

In order to determine the width of the divider, we had to find the dimension that permits the laminar flow of the ALD precursors without forcing the divider to be too close to the chamber walls. Our attempt to find this can be illustrated by Figure 2.3, which shows the dependence of the distribution of the normalized density distribution of gas molecules used in ALD (ρ_{ALD}) for a variable divider width w. Our simulation is based on precursor gas flowing from the inlet to the outlet with the operating assumption that no reaction occurs between the gas and the substrate for three different widths: (a) 7 mm, (b) 35 mm, and (c) 63 mm. Also, note that for all three cases the height of the divider is constantly set to 10 mm. The desired height for laminar flow is analyzed in the following paragraph; but before this is addressed, the laminar flow in this simulation only becomes well established at (c), when the inlet and outlet are covered to the point of looking like a lintel.

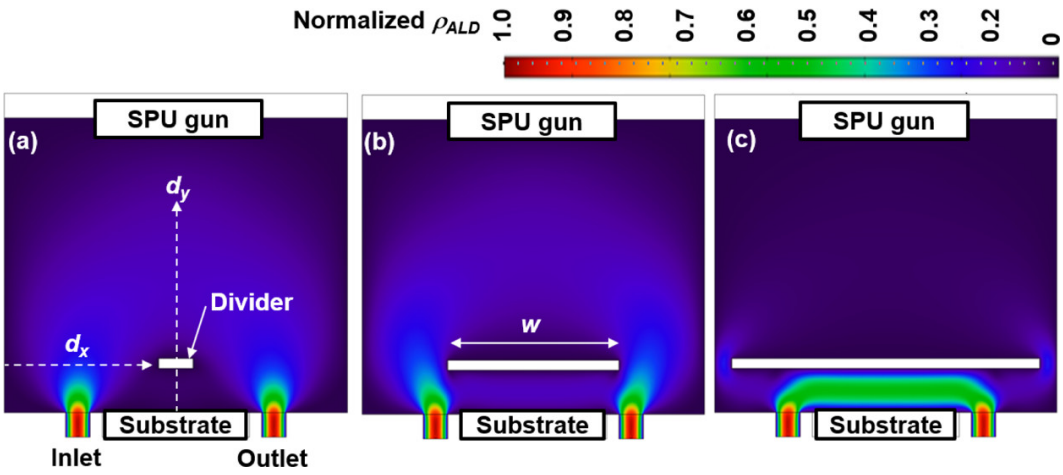

Figure 2.3: Gas flow pattern underneath the divider is shown for various w: (a) w = 7 mm, (b) w = 35 mm, and (c) w = 63 mm, respectively (Giraldo et al., 2020).

When the height of the divider d_y dictates the normalized ρ_{ALD} to be 1.0, then we will know what value to place the divider above the substrate. This is shown by the red arrow in the graph denoted by "development of a laminar flow" in Figure 2.4. At locations of d_y beyond the laminar flow, the precursor gas forms a dispersed cloud above the substrate that unevenly fills the chamber below the divider. Also, as seen in Figure 2.3, the laminar flow develops progressively as w increases, but the width must be at least 90% of the chamber, in order to obtain the desired density contrast below and above the divider used in CFD—FEA. Fortunately, even though the results are done under CFD—FEA with an original basis of a substrate with w_c = 20 mm, the design parameters in Table 2.1 are scalable for the potential real-world assemblage of different proportions. The simulated results may apply to the same capacity for the final mock-up used to run experiments, a machine with a diameter of 100 mm and a substrate of up to 50 mm in diameter.

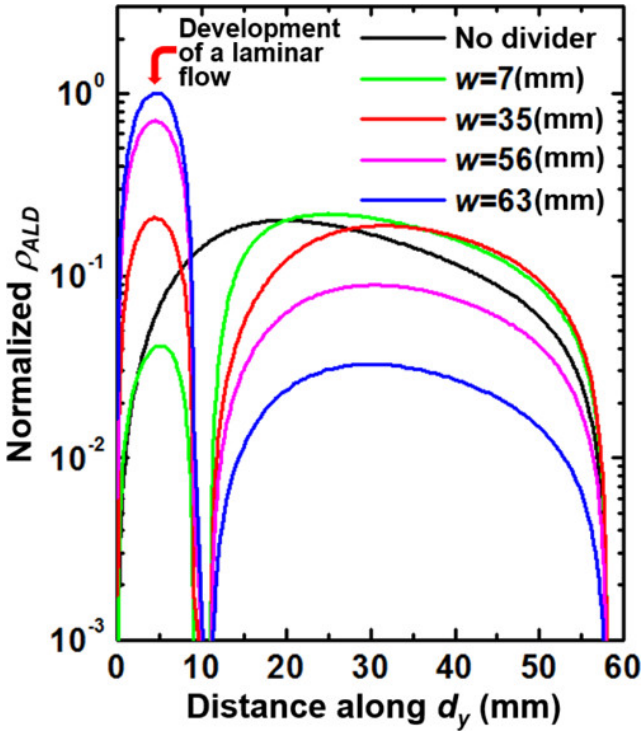

Figure 2.4: Variations of ρ_{ALD} as dependent on d_y the height of the divider for a specific divider width, indicating the progressive development of a laminar flow as w increases (Giraldo et al., 2020).

2.4 FASD Engineering

Moreover, principle reflections during CFD—FEA led us intending to use some 3-5 mm thick plate made of stainless steel (e.g. type 304) divider that would be inserted and retracted from inside the reaction chamber in a matter of a few tenths of a millisecond, hence its fast-acting nature. This hope was guided by the pre-supposition that the divider would not completely make physical contact with the reaction chamber when inserted, as a divider with the capability of moving in such a time frame would allow the control of the deposited species from the SPU gun to not deviate from expected results because transitionary insertions and retractions from SPU gun systems with conventional mechanical shutters were found to be in-

effective at controlling both the gas flow of ALD and the sputtered species of SPU.

Unfortunately, the real application of such a divider was unsuccessful and the ideal design we envisioned in CFD—FEA had to be scrapped. In future designs, this would achieve favorable results. However, the fundamental goal to show the hybridization of ALD and SPU processes in a single vacuum chamber was significant enough to move along with a slightly less than optimal reality, so a conventional mechanical gate valve that was driven with the time scale of a few seconds during insertion and retraction was chosen as a replacement. As a result, the electric ground potential of the divider is equal to that of the SALAD system (i.e. the substrate stage where the species is deposited has the equivalent electric potential), thus effectively isolating ALD and SPU processes both spatially and temporally.

3

Experimental Section

In this chapter, I discuss the experimental parameters used to design an AlO_x-Cu nanocomposite in the SALAD machine, with the goal being to deposit without cross-contamination. I first recap the properties of each deposition method that are required for such an operation to function properly. I proceed by then outlying the sequence of events in the chamber that would lead to there being a recipe for 300 layers of seven nanocomposite samples, each with different SPU-Cu thicknesses.

3.1 Properties of Materials

The series of deposition runs carried out by our lab to demonstrate the capabilities of unifying ALD and SPU in a single vacuum chamber through SALAD used thin film structures made of the dielectric material AlO_x and the metallic material Cu stacked atop one another. AlO_x was an easy choice for these experiments because of its maturity as an ALD dielectric material, but the choice for Cu carried more theoretical weight. Silver (Ravindran et al., 2006; Gorbunova et al., 2017) and gold

(Maya et al., 1995; Figueiredo et al., 2011; Lozovski 2016; Figueiredo et al., 2014) are close to our goal of using a metallic material commonly used as inclusions embedded in dielectric materials in order to explicitly tailor their optical properties, but Cu was chosen instead because its free electron density is higher than either of the two. Aluminum could replace Cu but it was avoided to prevent AlO_x from forming after it was deposited and exposed to the ALD process (oxidation from the exposure to the H_2O precursor), which if it occurred would obfuscate our goal of having distinct interfaces.

Additionally, Cu forms a variety of oxides including Cu_2O, CuO, and Cu_4O_3 that serve as significant modifiers of the dielectric properties of ALD-AlO_x by behaving as a band insulator (Kazimierczuk et al., 2014), a charge-transfer insulator (Ghijsen et al., 1988), and a mixed-valence compound consisting of Cu_2O and CuO, respectively (Meyer et al., 2012). Beyond this, these oxides through various analytical methods can be distinguished from ALD-AlO_x and used to study intermediate phases made by alternating depositions of ALD-AlO_x and SPU-Cu.

3.2 Deposition Parameters for AlO_x-Cu Nanocomposites

The specific deposition parameters summarized in Tables 3.1 and 3.2 were explicitly obtained by separately calibrating ALD and SPU in the SALAD system. By achieving the necessary deposition rate required for designing a single SPU step

that delivered a quantified level of Cu, we were able to set the necessary parameters needed to coat a uniform sputtered layer alongside the self-limited layer of AlO_x. In other words, SPU thickness is the only alterable layer because one layer of ALD AlO_x plateaus at a certain thickness; so even if the trimethylaluminum (TMA) precursor is pumped indefinitely inside the chamber, there are no more bonds provided by the H_2O precursor past a certain point for TMA to attach.

Consequently, the self limiting deposition rate is represented by $\Gamma_{ALD} = 0.13$ nm/cycle for ALD-AlO_x. Whereas, the deposition rate of the SPU process yields units for the growth rate in time, $\Gamma_{SPU} = 0.04$ nm/s. SPU benefits from not needing a 'primer' so to speak, so if left running continuously on say an infinitely robust target, the sample would permanently gather Cu layers until it filled the chamber. More to the point, the total amount of SPU-Cu is simply dictated by specifying a unique duration (t_{SPU}). The deposition rates for both materials were found using a FilmTek 4000 spectroscopic reflectometry/ellipsometry equipped with a Halogen/Deuterium UV-visible.

Table 3.1: Summary of ALD Conditions Used to Deposit AlO_x–Cu Nanocomposite Thin Film Samples

ALD Parameters	
aluminum precursor	$Al(CH_3)_3$
oxygen precursor	H_2O
purge/carrier gas	argon
duration of an $Al(CH_3)_3$ pulse	80 ms
duration of a H_2O pulse	150 ms
purge duration after an $Al(CH_3)_3$ pulse	10 s
purge duration after a H_2O pulse	10 s
purge/carrier gas flow rate	20 sccm

Table 3.1: Continued.

ALD Parameters	
deposition temperature	150 °C
base pressure	0.14 Torr
G_{ALD}	0.13 nm/cycle

Table 3.2: Summary of the SPU Conditions Used for Depositing the AlO_x–Cu Nanocomposite Thin Film Samples

SPU Parameters	
target material	Cu (purity 99.999%)
dc power density	5 W cm^{-2}
SPU gas	argon
deposition temperature	150 °C
deposition pressure	0.24 Torr
deposition rate G_{SPU}	0.04 nm/s

3.3 A Single Deposition Run

A single SALAD deposition cycle is thought to be one SPU step inserted between two ALD cycles. In Figure 3.1, this is illustrated by relating the change of the background pressure in the chamber to time, so the red horizontal arrows indicate the t_{SPU} needed for our desired layer to be 3.0 seconds. Or more specifically, a single SALAD cycle for this demonstration is considered to be one 3.0 second layer of SPU-Cu after one layer of ALD-AlO_x. A total of three SALAD layers occur for the complete domain in the figure, even though there are 300 SALAD cycles used to form the aggregate of our experiment's architecture.

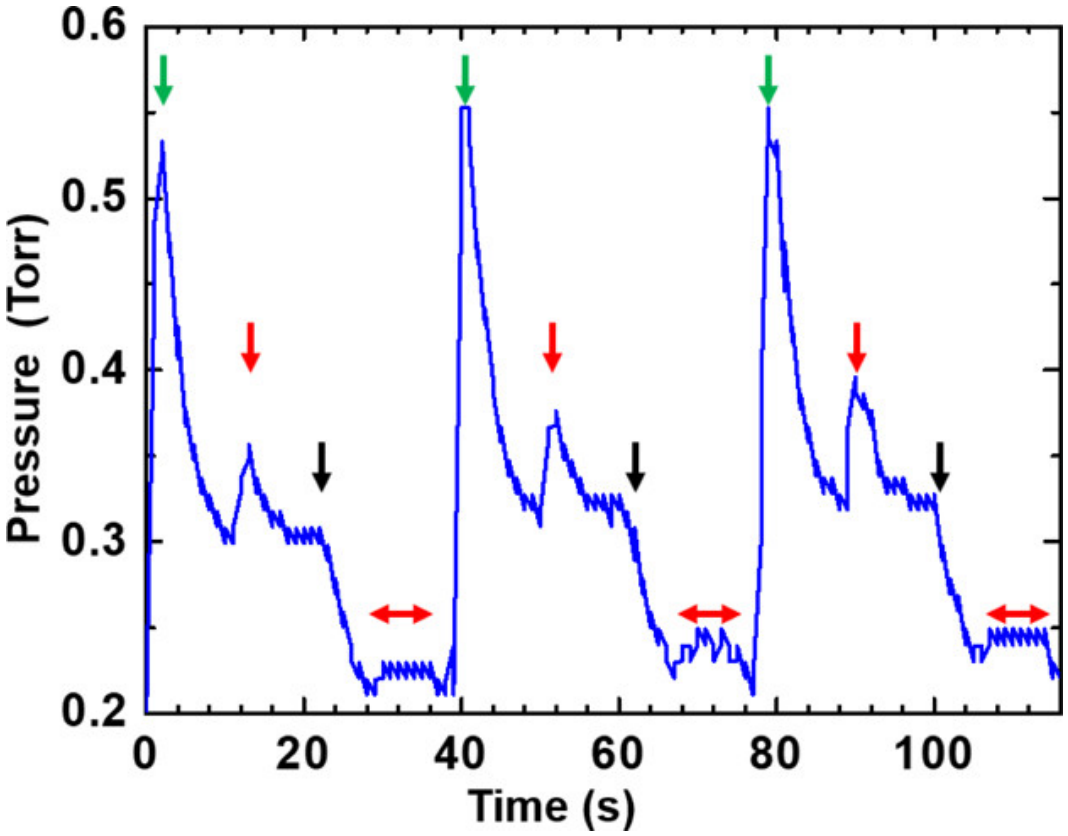

Figure 3.1: Time-progressive change in the background pressure in the SALAD system shows three SALAD cycles recorded during the deposition of one of the AlO_x–Cu nanocomposite thin film samples used in the study. Each SALAD cycle is comprised of an $Al(CH_3)_3$ pulse denoted by the green vertical arrows, a purge of $Al(CH_3)_3$, an H_2O pulse denoted by the red vertical arrows, a purge for H_2O, and an SPU duration indicated by the red horizontal double-head arrows. A sharp drop in pressure indicated by the black vertical arrows results from temporarily stopping the flow of argon carrier gas used in the preceding ALD step. Regardless of the total number of SALAD cycles performed in a single SALAD run, the Cu SPU cathode was kept turned on during all single deposition runs performed in the experiment (Giraldo et al., 2020).

The preparation for a singular SALAD layer begins by first enabling the SPU cathode to 24 V, which in turn ignites the magnetron plasma at the Cu SPU target when the inert gas is introduced. The vacuum chamber must be pumped down to around 150 mTorr in order to activate plasma and the divider must be closed, isolating the plasma from the substrate. From here, we run the plasma in the chamber for at

least ten minutes to remove impurities from the surface of the Cu SPU target and to stabilize the plasma. Once these initial conditions are met, one can input whatever desired amount of cycles that is to be performed through the SALAD user interface that was coded in LabVIEW. Regardless of the cycle amount inputted into the recipe, the SPU cathode is engineered to continuously induce plasma during every deposition sequence, even when the divider is closed and ALD-AlO_x is being deposited.

Figure 3.1 specifies in detail the sequential steps needed to produce a single SALAD layer that goes beyond just SPU, as shown principally by the $Al(CH_3)_3$ precursor pulse indicated by the green vertical arrow. Following the spike, is a purge for $Al(CH_3)_3$, an H_2O pulse marked by a red vertical arrow, a purge for H_2O, and a subsequent SPU step that is indicated by a double-headed horizontal red arrow that lasts as long as t_{SPU} is specified for (in this case 3 s econds). Before activating the SPU step, SALAD requires the unique operation after the purge of H_2O to, as observed by the sudden drop in pressure indicated by the black arrow, stop the flow of argon carrier gas for the ALD-AlO_x purge. This must occur because the perpendicular laminar flow relative to the substrate surface blocks SPU species from reaching the thin film surface, and in some sense, it acts as an impenetrable barrier that stops the SPU-Cu thin film.

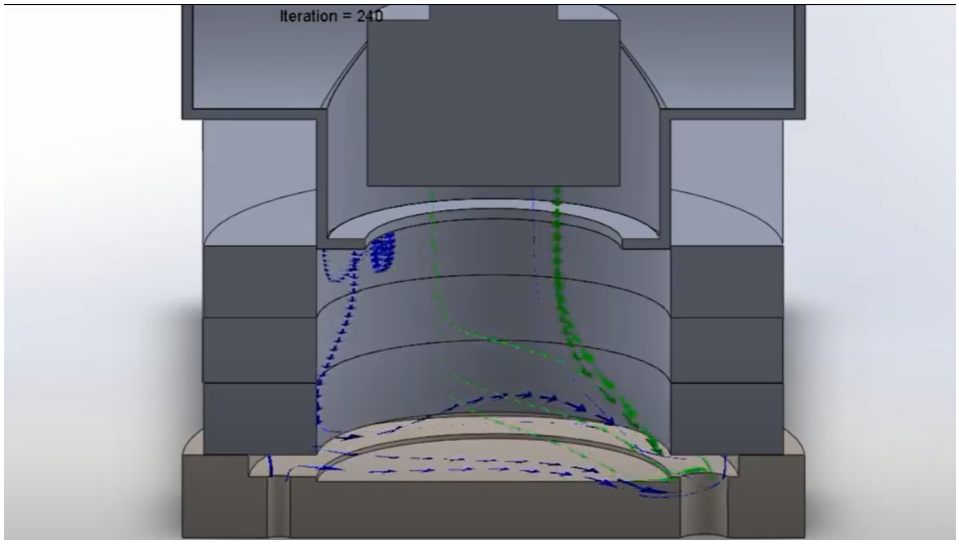

Figure 3.2: A cursory analysis in SolidWorks was produced to illustrate the impenetrable barrier that stops the SPU-Cu thin film growth. The blue material represents the argon pumped through the inlet on the left and the green material represents SPU-Cu. Both flow towards the outlet to the right of the chamber, so no SPU-Cu is able to reach the substrate because it is blocked by the incoming argon.

In an effort to make the launch of SALAD as simple as possible, an SPU step was chosen to follow after a full ALD cycle had passed because this sequence avoids interrupting the growth of a complete ALD layer. Technically, it is easily programmable to have SPU occur after an $Al(CH_3)_3$ or H_2O pulse/purge, but this is avoided to ensure the complete isolation of a finished ALD cycle and the beginnings of an SPU layer. This sequential design in tandem with the banishment of inlet material, specifically argon, during SPU were the required assumptions used to produce and keep consistent the results in Figure 2.2 via CFD—FEA.

3.4 Producing Samples

A total of 300 SALAD cycles was fixed for all samples in the series of AlO_x-Cu nanocomposite thin films deposited on glass substrates (Corning 2497) by repeating the SALAD cycle of one ALD-AlO_x layer that is followed by another layer of SPU-Cu. The step size for a specific t_{SPU} varied in the range from 1.3 to 7 seconds to generate a nominal thickness equivalent to 0.05 - 0.28 nm under a deposition rate Γ_{SPU} = 0.04 nm/s. Preceding the deposition, nothing was added nor cleaned to the nature of the glass substrates, as they were directly applied to the chamber after being pulled from their original container.

Before we were able to confirm the results in a way that denies any shadow of a doubt in regards to the body and interface structures, we had to make a couple of assumptions that are confirmed later in the paper by ellipsometry, atomic force microscopy (AFM), and energy-dispersive X-ray spectroscopy (EDS). The first is that a single SALAD cycle yields a layer of ALD-AlO_x with a thickness of 0.13 nm followed by a layer of SPU-Cu with a nominal thickness of 0.04 nm/s x t_{SPU} and the second is that no intermixing of ALD layers or SPU layers transpires throughout the run, thereby providing the necessary framework to quantitatively distinguish the prepared samples. As it were otherwise, then there would be no such thing as well-defined layers, but instead a thin mixture of material made of more disorder than what could be considered a heterogeneous order.

More analysis to confirm this assumption is needed by carrying out detailed struc-

tural and chemical analysis of the samples; but for the general purposes of this paper, the AlO_x-Cu nanocomposite thin film samples prepared with varied t_{SPU} are contemplated as $(AlO_x)_n(Cu)_m$ where n/m = (Γ_{ALD} x 1 ALD cycle)/(Γ_{SPU} *t_{SPU}) and n+m = 1. Table 3.3 shows the prepared seven variations of AlO_x-Cu nanocomposite thin film samples under this method by solving for n and m for a given t_{SPU}. Additionally, a 120 nm thick SPU-Cu sample without ALD-AlO_x and a 30 nm thick ALD-AlO_x without SPU-Cu were prepared to serve as reference samples. Altogether, the SALAD experiment in the paper consists of nine different versions of thin film structures that will undergo analysis of their structural and optical integrity.

Table 3.3: n and m Calculated for Various tSPU Used in the Experiment Providing Seven Variations of AlO_x–Cu Nanocomposite Thin Film Samples Identified by m

t_{SPU}	n	m	d_{ALD}	d_{SPU}
1.3	0.71	0.29	15	39
2	0.62	0.38	24	39
3	0.52	0.48	36	39
4	0.45	0.55	48	39
5	0.39	0.61	60	39
6	0.35	0.65	72	39
7	0.32	0.68	84	39

4

Results and Discussion

Our main results come from the reflectance spectra data. Before I begin there, I first declare from the results of energy-dispersive X-ray spectroscopy and AFM results that a full AlO_x-Cu nanocomposite layer develops without cross-contamination or impurities. After the layer has been identified to be of expected architecture, reflectance spectra are measured with a monochrometer. The data is then used to analyze compositional information that may have been lacking in the calculated reflectance spectra.

4.1 EDS Structural Results

The structural elements that describe the atomic order of SALAD thin films were analyzed by a couple different methods. The first is an energy-dispersive X-ray spectroscopy (EDS) in a scanning electron microscope. This was used to obtain the atomic composition of the expected chemical elements that are predominantly present in the samples: Cu, oxygen (O), aluminum (Al), and carbon (C). Settings for

such an analysis were chosen to satisfy the optimal outcome of EDS; these quantitative results are achieved by using enough beam energy to allow for an overvoltage (anything beyond 10 kV is an overvoltage if one is concerned with interaction volumes in the micron range) that will optimize the production of characteristic K-line emissions for the specified elements of interest.

Additionally, for the X-ray emissions to produce reliable count rates used for quantification, the beam current is adjusted to balance the minimization of absorbed emissions from lighter elements and the obtainment of an adequate overvoltage. If the analysis is performed without these considerations, the samples may be subject to structural damages that warp the original nature of the beam, potentially producing weak and inadequate peak intensities that offer lesser results for quantification. Ergo, the net settings observed included an acceleration voltage of 15 kV and an electron current of 1.6 nA.

Figure 4.1 shows the weight percentages (wt $\%$) of the chemicals listed above plotted as a function of m. The wt $\%$ of Cu (red solid line) is isolated in (a), and the wt $\%$ of O (blue solid line), Al (orange solid line), and C (green solid line) are shown in (b). The gist of graphs (a) and (b) demonstrate to us that the growth rate for SPU is time-dependent and the growth rate of ALD, a self-limiting procedure, is cycle dependent. We see the composition as it changes with m, so as we increase the copper in each sample we can see an increasing linear relationship. Now, this seems fairly obvious, but this tells us something very important – that AlO_x and Cu are separately deposited. If this was not upwardly linear then this would represent

a messy intermixture of material layers.

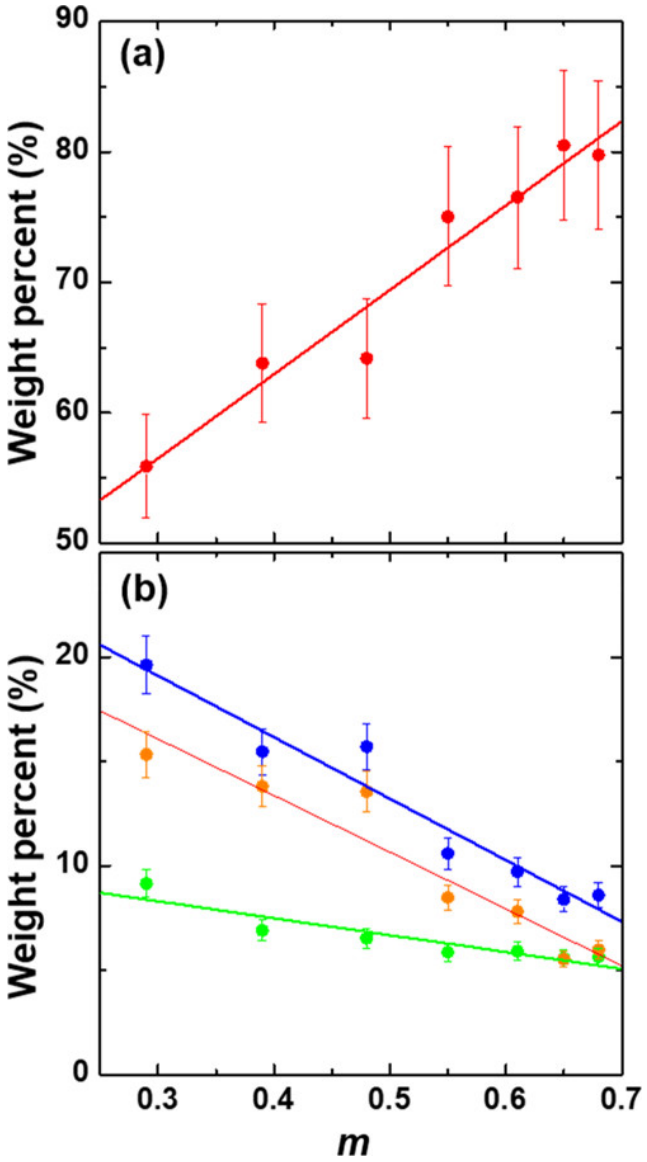

Figure 4.1: Weight percent (wt %) of Cu in (a) and O (blue solid line), Al (orange solid line), and C (green solid line) in (b). The wt (%) of these chemical elements were obtained by using EDS spectra collected on the AlO_x–Cu nanocomposite thin film samples prepared with various m (Giraldo et al., 2020).

Unfortunately, the same cannot be said about the downward linear relationships in (b). Ideally, these plots should be constant, but we surmise that the qualitative anal-

ysis from EDS is somewhat questionable because we used an e-beam to excite the sample; so since we lack the knowledge to know how far the beam penetrates, we deduced that the signal coming from Al and O could have been blocked by Cu. We do know that if the thickness of the sample increases with m and the ALD-AlO_x is fixed to 300 for all of the samples, then as m increases so does the probability that the signal would be blocked by Cu. We believe that even though our measurement is shy of perfection, the downward linear relationship greatly hints our structural assumption to be in the ballpark.

As for the slightly decreasing trend of C from 8 to 5 wt $\%$ as m increases, we viewed this as being consistent with the relative decrease in C carrying ALD-AlO_x precursor trimethylaluminum, $Al(CH_3)_3$. This could also be because AlO_x is known to easily contaminate C. Under a perfect system, there would not be any carbon left in the chamber because it would have been completely purged while they were under the form of methane (CH_3). Overall, some potential discrepancies could be resolved by better measuring the absolute atomic concentration with machines like secondary ion mass spectroscopy or X-ray photoelectron spectroscopy; but we feel that under the appropriate analysis described so far, the two deposition processes had a minimum influence on each other so they are effectively isolated during deposition sequencing.

4.2 Effective Medium Approximation

Coordinating the focus of this demonstration was guided by our interest in the potential optical properties of an AlO_x-Cu nanocomposite thin film, which was expected to adjust per variation of SPU-Cu in the samples represented by m. We captured measurements of the reflectance spectra (R spectra) to emphasize the supposed unique dielectric properties of the experimental samples, and we used the effective medium approximation (EMA) to assess the spectral reflectance by using spectroscopic ellipsometry to extract the dispersion of permittivity. For example, the produced AlO_x-Cu nanocomposite thin film was treated as an effective medium that consisted of multiple stacks of a metal-dielectric pair. We felt it logical to use EMA because, in principle, the layers of the Cu and AlO_x layer, which are quantized in the range of 0.13-0.28 nm, are significantly smaller than the wavelengths of light used in the measurement of R spectra (Smith & Pendry, 2006).

Notwithstanding initial reasoning, our EMA assessment produced a spectral refractive index and extinction coefficient that was nonsensical to the point of us proclaiming it as physically meaningless when compared to the measured R spectra obtained experimentally by our study. EMA may have gone awry for a few reasons. First off, the way by which we implemented EMA may not have been an accurate depiction of the structural details of the AlO_x-Cu nanocomposite thin film samples. Our assumption was specifically that the thin films consist of multiple stacks of a metal-dielectric pair with smooth two-dimensional interfaces geometrically parallel to the surface of the substrate.

Where the most likely outlier may be is within the true nature of the SPU thin film composition. There may be unaccounted-for vacancies or clumps that are subtle yet significant enough to change the EMA. A different explanation could be that the continuous Cu layer may not form on the surface of ALD-AlO_x during an SPU duration, regardless of a specific period of time that is preset for t_{SPU}. Therefore, microscopic structural details must be obtained in order to establish an effective medium description that suitably represents the reality of our thin film samples, preferably through transmission electron microscopy.

Plus, EMA is often found to be an approximation not capable of producing reliable results in metal-dielectric multi structures, which unfortunately is the type of structure we designed for this experiment. This is usually the case when the surface plasmon polariton excitations create additional electric fields that vary the scale interfaces and the nominal thickness of the metal and dielectric structures, despite the thickness of the material being significantly smaller than the wavelengths used for R spectra measurement (Elser et al., 2007; Iorsh et al., 2012; Kidwai et al., 2011; Orlov et al., 2011; Kidwai et al., 2012). For the posterity of the lab, it is likely that we will see an optical assessment method that obtains the dependence of complex reflection amplitude r on wavelength by analyzing the R spectra experimentally obtained. This in combination with an analysis of the same desired quantity but through the Kramers-Kronig relation to determine the complex dielectric function may solve the missing links that finalize the structural classification of AlO_x-Cu nanocomposite thin films (Jahoda 1957).

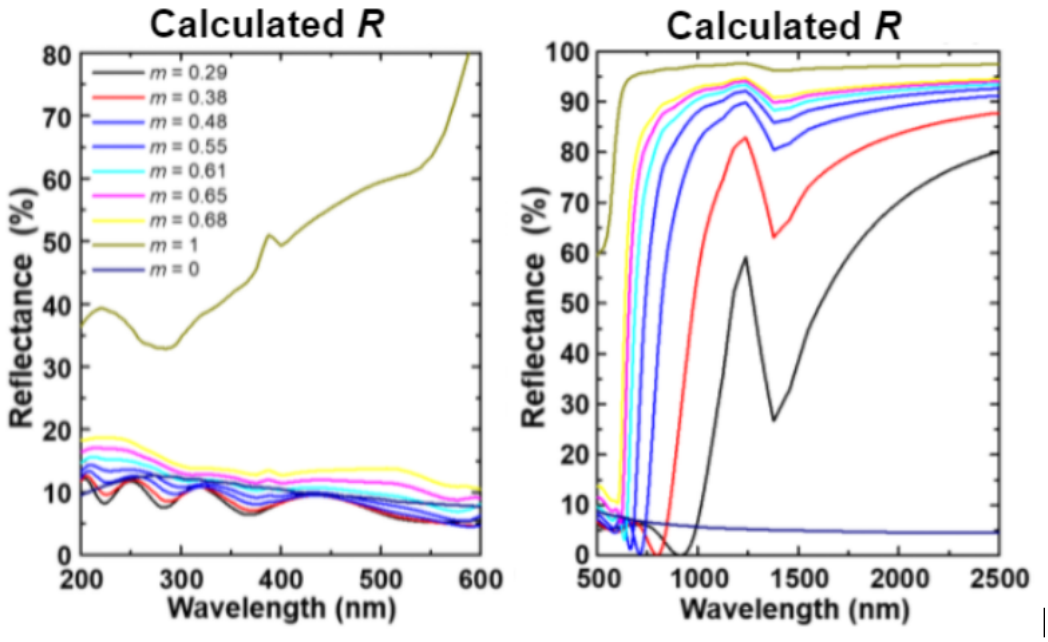

Figure 4.2: This reference of R Spectra was calculated with the conventional effective media approximation. Measured results vary dramatically, hinting that there may be a newer model outside of classical analysis to determine a SALAD metal-dielectric nanocomposite (Sands et al., 2020).

4.3 Statistical Surface Roughness

An atomic force microscope (AFM) obtained the statistical surface roughness of the AlO_x-Cu nanocomposite thin film samples needed for us to assess whether or not the layers were indicative of a uniform structure. We performed this measurement with a non-contact probe and a scanning frequency of 1 Hz over an area of 1 μm x 1 μm with the number of imaging pixels being 512. Beginning with these conditions, we compounded a root mean square (rms) roughness collected by the resulting AFM data as a function of m, which is represented by Figure 4.3. To ensure statistical validity, each data point on the graph represents an average of seven AFM scans on one unique m sample. The error bars at each point m reflect the

standard deviation associated with the multiple scans. Beyond this, we fitted an exponential trend line across all of the data points from the first point at m = 0.29 (1.3 s) to the last point at m = 0.68 (7 s), as shown by the dotted curve.

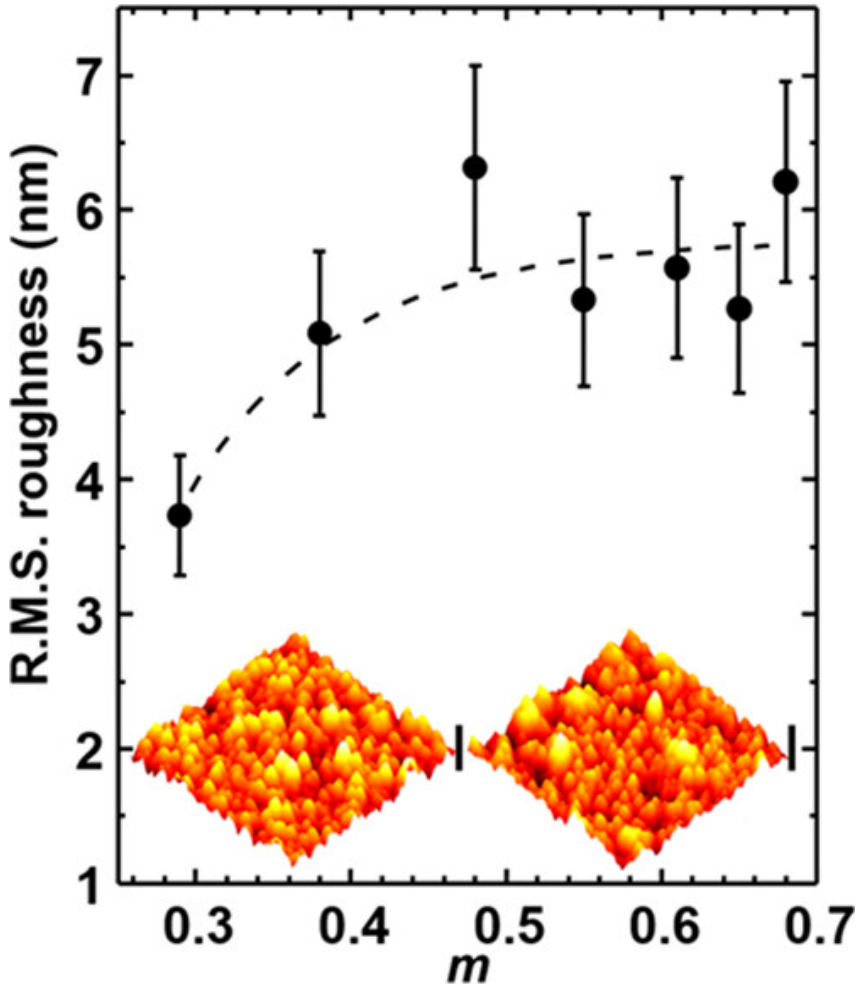

Figure 4.3: rms roughness obtained by AFM is plotted as a function of m. A single data point represents the average over multiple AFM scans on a sample with a specific m . The error bar represents the standard deviation collected for each data point. The broken line serves as a trend line resulted from fitting an exponential function to the data points. The inset shows two representative perspective-views of samples with m = 1.3 s (left) and m = 7 s (right) collected across 1 mm × 1 mm area by AFM, respectively. The vertical scale bars represent 27 nm (left) and 37 nm (right) along the z-axes (i.e., height), respectively (Giraldo et al., 2020).

The roughness topography in the inset shows a perspective view of samples m = 0.29 (left) and m = 0.68 (right) collected across the area 1 μm x 1 μm. Vertical

scale bars represent 27 nm (left) and 37 nm (right) along the height, given by the z-axis. Beginning with the reference points of the rms roughness to be respectively 0.15 nm and 0.95 nm for ALD-AlO_x (m = 0) and SPU-Cu (m = 1), the trend line then indicates that the rms roughness increases significantly from 0.15 nm at m = 0 to 3.73 nm at m = 0.29 and 5.08 at m = 0.38. At the level beyond m = 0.38, the roughness saturates. If the AFM results did not plateau, then we would not have been able to use R spectra to provide insights into the unique structural and electronic characteristics of the SALAD AlO_x-Cu nanocomposite thin film samples.

4.4 Reflectance Spectra

Initially, we assumed that the effective medium approximation was linearly dependent, which resulted in the calculated R spectra in Figure 4.2, but we were surprised to find that we could not replicate the measured reflectance with the summation of the reflectance from Cu and AlO_x. Currently, we do not know the predictor needed to arrive at the collected data of our varying SALAD layer compositions, so finding a new approximation that accounts for this unknown is one of the many goals in research.

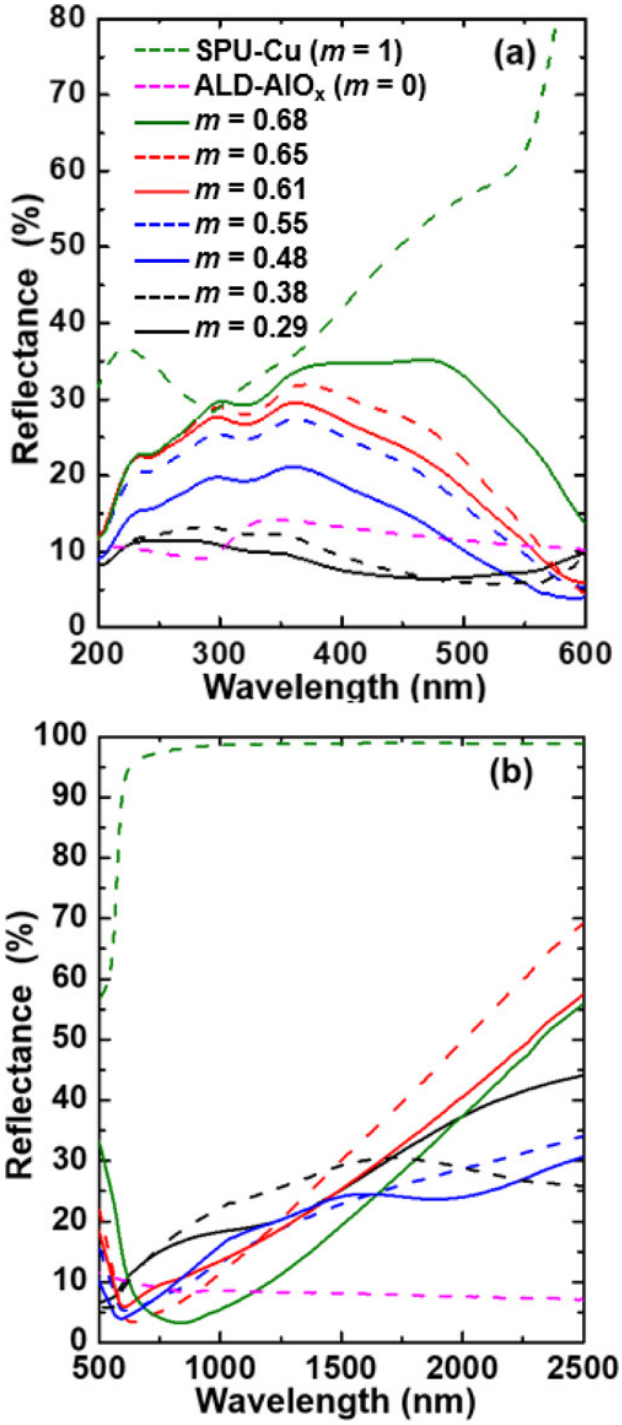

Figure 4.4: Reflectance spectra of the AlO_x–Cu nanocomposite thin film samples prepared with various m along with those collected from SPU Cu (m = 1) and ALD AlO_x (m = 0). The reflectance spectra are plotted over two different ranges: (a) 200–600 and (b) 500–2500 nm to highlight features distinctive in their respective ranges (Giraldo et al., 2020).

That being said, there is still valuable information that can be interpreted from what

we found to be true about the SALAD samples. Before I address this, I'll begin by elaborating on the methodology of measurement used to arrive at conclusions. The R spectra of seven samples with various m in the range of 0.29-0.68 was collected at room temperature using an unpolarized white light source combined with a monochrometer. Two reference samples are also displayed in the Figure 4.4 to show the general R dispersions at a pure 120 nm bulk of SPU-Cu (m=1) and 30 nm of amorphous ALD-AlO_x (m=0). The two ranges of wavelength match the profile used in our calculated spectra, i.e. 200-600 nm in (a) and 500-2500 nm in (b). The split between shorter wavelengths and longer wavelengths at 600 nm is meant to represent the plasma reflection edge of bulk Cu that occurs $\sim$560 nm.

4.5 Reflectance of the Shorter Wavelengths

Essentially, the features in Figure 4.4a are strongly influenced by interband transitions rather than contributions associated with free electrons, which are the main influencing factor of Figure 4.4b. More specifically, the absorption coefficient of bulk Cu in the shorter wavelength spectra was found to exhibit features that originate from three interband transitions at various symmetry points: L2–L1, X5–X4, and L3-Fermi surface (Segall, 1962). Therefore, the wavy contour of the spectra line is most likely associated with the progressive formation of well-defined Cu electronic bands. Another perspective to add to this feature is that the increase in the total volume of Cu as m increases by a fraction reinforces the tactical control of the SALAD system on delivering SPU-Cu without contamination because the interband transitions sharpen with each progression.

Various chemical states of Cu (e.g., copper oxides and copper hydroxide) may be present, in addition to metallic Cu, in the AlO_x–Cu nanocomposite thin film samples because of the presence of hydroxide and hydroxyl radicals in the deposition environment both in gas phase and on the growing surface after the completion of a single ALD cycle using H_2O as a precursor. Thus, the statement "the progressive formation of well-defined Cu electronic bands" needs to be further clarified and validated by performing such complementary characterization as Raman scattering spectroscopy, X-ray photoelectron spectroscopy, and electron-energy-loss-spectroscopy combined with transmission electron microscopy to elaborate a physical and chemical picture of Cu–either forming a continuous or noncontinuous layer effectively separated by a single ALD-AlO_x layer–to further address the formation of electronic bands directly resulting in unique finger prints seen in the R spectra . Controlling the chemical states of Cu in the AlO_x–Cu nanocomposites is critical in designing, for instance, hyperbolic metamaterials based on metal–dielectric multi layers (Giraldo et al., 2020; Poddubuny 2013).

4.6 Reflectance of the Larger Wavelengths

In the larger wavelength group of Figure 4.4b past the plasma reflection edge of bulk Cu, we expected the dispersion of R collected from the AlO_x-Cu nanocomposite thin film to reflect a precise blending of the two constituent materials. The free electrons in the Drude-Lorentz theory that do not experience a restoring force play a major role in determining the complex dielectric constants (ex. extinction

coefficient) for Cu within the larger wavelength group to determine the measured R spectra. Friction damping or the retarding action of the surrounding medium represented by F_y sets up the equations of motion for the displacement of the free electrons described in the theory. Usually, F_y is set to zero in order to explain the R spectrum of SPU-Cu (m = 1) being close to 100%.

Unlike the result of Figure 4.4a where it is apparent that as m increases the reflectance becomes more like the reflectance of Cu, there is no distinct tendency as m changes in Figure 4.4b. Interestingly, there is a distinct adjustment between the calculated and the measured reflectance spectra because the sharp increase in the calculated spectra is nonexistent in the measured one. At most, it is a gradual increase. Regardless, it appears that perhaps F_y should not have been set to zero for the samples of m = 0.29–0.68, for it seems that F_y is meant to be much larger in the AlO_x-Cu nanocomposite thin films.

Another possibility is that the interband transition where the plasma reflection edge takes place somehow extends well above the mark of ~560 nm, suggesting that ALD-AlO_x layers may have given rise to additional transitions associated with SPU-Cu in the AlO_x-Cu nanocomposite because of the alterations on the density in 3d and 4s bands of Cu. All of this caught us by surprise because we used effective media approximations to calculate the expected reflectance of these varying compositions and they did not warn that any of this would occur, hinting that the classical tool used for approximation did not extend to this new frontier and that a new one needs to be developed.

4.7 Reflectance Discussion

Contributions to the unique R spectra in Figure 4.4 may be predicated by the macroscopic level rather than the microscopic level. For instance, the fact that the two types of layers have different values for their refractive indexes may be the reason why there is optical interference. It seems possible to neglect the impact of such a distortion because the thicknesses of each ALD-AlO_x and SPU-Cu layer in the AlO_x–Cu nanocomposite thin film samples is much smaller than a quarter of the wavelength of the light used to measure the R spectra, destructive and constructive interferences by which conventional distributed Bragg reflectors and band-pass filters operate are not relevant.

Another level of interference to the measured R spectra may have occurred because of the skin effect. Often used in the discussion of ac conductivity in metal, the skin depth of Cu is estimated to be 2.7–5.9 nm using the conventional formula (Hwang & Turlik 1992) for electromagnetic waves with respective wavelengths of 500–2500 nm relevant to our experiment. Note that the thickness of the skin depth is up to two orders of magnitude larger than the thickness of a single SPU-Cu layer in the nanocomposite, so it seems more likely than not that the skin depth has very little impact on the optical results.

In the Maxwell Garnett approximation, a complex medium—effective medium—is assumed to exhibit effective permittivity approximated in terms of the permittivity and volume fractions of the independent constituents of the complex medium

(Koledinstseva et al., 2006). Moreover, the Maxwell Garnett approximation is often described as effectively approximating the interaction between electromagnetic waves and such complex mediums as a colloidal solution of metallic particles. This may be relevant because, of course, SALAD is capable of nanocomposites A_yB_{1-y} made of a dielectric element A that contains metal inclusions made of element B; wherein the complex optical characteristics may produce noticeable reflectance variations if the metal-dielectric compositional ratio y is in the range of 0.2–0.8 (Cohen et al., 1973). We acknowledge that this is possible, but we believe that the random distribution of metallic particles for thin film growth on the dielectric material, which is assumed in the approximation, does not take into account the interchanging periodicity (i.e., ALD-AlO_x and SPU-Cu layers being stuck on top of each other) of the SALAD sample.

5

Conclusion

Modeling the chamber's gas flow through 2D computational fluid dynamics with finite-element analysis allowed us to optimize our SALAD design parameters (divider width, chamber width, and throw gun distance) to accomodate for ideal thin film growth environments of sputtering and atomic layer deposition within one chamber. Once constructed, complex analysis of atomic force microscopy and energy dispersive X-ray spectroscopy confirm that our vision of creating contamination-free, distinct, and uniform interchanging metal-dielectric layers are possible with SALAD. While successful in practical applications, the hybridized production of elements that are conventionally treated as separate entities confronts the limits of our current understanding. Inconclusive efforts to approximate or simply interpret the optical results of an ALD-AlO_x and SPU-Cu nanocomposite prove we still have more to learn from SALAD's charisma. Pioneering beyond the verge of what we do know will require detailed structural analysis beyond our current abilities; but we are confident that with enough out-of-the-box thinking, the field of thin films may become richer as SALAD matures.

References

Cohen, R. W., Cody, G. D., Coutts, M. D., & Abeles, B. (1973). Optical properties of granular silver and gold films. *Physical Review B, 8*(8), 3689-3701. doi:10.1103/physrevb.8.3689

Elliot, A. J., Malek, G. A., Lu, R., Han, S., Yu, H., Zhao, S., & Wu, J. Z. (2014). Integrating atomic layer deposition and ultra-high vacuum physical vapor deposition for in situ fabrication of tunnel junctions. *Review of Scientific Instruments, 85*(7), 073904. doi:10.1063/1.4890286

Elser, J., Podolskiy, V. A., Salakhutdinov, I., & Avrutsky, I. (2007). Nonlocal effects in effective-medium response of nanolayered metamaterials. *Applied Physics Letters, 90*(19), 191109. doi:10.1063/1.2737935

Figueiredo, N. M., Kubart, T., Sanchez-García, J. A., Escobar Galindo, R., Climent-Font, A., & Cavaleiro, A. (2014). Optical properties and refractive index sensitivity of reactive sputtered oxide coatings with embedded au clusters. *Journal of Applied Physics, 115*(6), 063512. doi:10.1063/1.4861136

Figueiredo, N., Carvalho, N., & Cavaleiro, A. (2011). An XPS study of au alloyed al–O sputtered coatings. *Applied Surface Science, 257*(13), 5793-5798. doi:10.1016/j.apsusc.2011.01.104

Fryauf, D. M., Phillips, A. C., & Kobayashi, N. P. (2015). Corrosion barriers for silver-based telescope mirrors comparing PEALD and PVD of AlOx. *MRS Proceedings, 1805*. doi:10.1557/opl.2015.686

Ghijsen, J., Tjeng, L. H., Van Elp, J., Eskes, H., Westerink, J., Sawatzky, G. A., & Czyzyk, M. T. (1988). Electronic structure ofcu2o and cuo. *Physical Review B, 38*(16), 11322-11330. doi:10.1103/physrevb.38.11322

Giraldo, B., Fryauf, D. M., Cheney, B., Sands, J. H., & Kobayashi, N. P. (2020). Demonstration of Sputtering Atomic Layer Augmented Deposition: Aluminum Oxide–Copper Dielectric–Metal Nanocomposite Thin Films. *ACS Applied Materials & Interfaces, 12*(12), 14280-14288. doi:10.1021/acsami.9b18628

Gorbunova, M., Lemkina, L., Lebedeva, I., Kisel'kov, D., & Chekanova, L. (2017). Synthesis and potential applications of silver—porous aluminium oxide nanocomposites as prospective antiseptics and bactericides. *Journal of Materials Science: Materials in Medicine, 28*(3). doi:10.1007/s10856-016-5841-z

Greene, J. E. (2017, September 08). Review article: Tracing the Recorded History of Thin-Film Sputter Deposition: From the 1800s to 2017. *Journal of Vacuum Science & Technology A: Vacuum, Surfaces, and Films, 35*(5), 05c204. doi:10.1116/1.4998940

Guo, Z., Li, H., Chen, Q., Sang, L., Yang, L., Liu, Z., & Wang, X. (2015). Low-temperature atomic layer deposition of high purity, smooth, low resistivity copper films by using amidinate precursor and hydrogen plasma. *Chemistry of Materials, 27*(17), 5988-5996. doi:10.1021/acs.chemmater.5b02137

Hwang, L., & Turlik, I. (1992). A review of the skin effect as applied to thin film interconnections. *IEEE Transactions on Components, Hybrids, and Manufacturing Technology, 15*(1), 43-55. doi:10.1109/33.124191

Iorsh, I., Poddubny, A., Orlov, A., Belov, P., & Kivshar, Y. S. (2012). Spontaneous emission enhancement in metal–dielectric metamaterials. *Physics Letters A, 376*(3), 185-187. doi:10.1016/j.physleta.2011.11.001

Jahoda, F. C. (1957). Fundamental absorption of barium oxide from its reflectivity spectrum. *Physical Review, 107*(5), 1261-1265. doi:10.1103/physrev.107.1261

Kalutarage, L. C., Clendenning, S. B., & Winter, C. H. (2014). Low-Temperature Atomic Layer Deposition of Copper Films Using Borane Dimethylamine

as the Reducing Co-Reagent. *Chemistry of Materials, 26*(12), 3731-3738. doi:10.1021/cm501109r

Kazimierczuk, T., Fröhlich, D., Scheel, S., Stolz, H., & Bayer, M. (2014). Giant Rydberg excitons in the copper oxide cu2o. *Nature, 514*(7522), 343-347. doi:10.1038/nature13832

Kidwai, O., Zhukovsky, S. V., & Sipe, J. E. (2011). Dipole radiation near hyperbolic metamaterials: Applicability of effective-medium approximation. *Optics Letters, 36*(13), 2530. doi:10.1364/ol.36.002530

Koledintseva, M. Y., DuBroff, R. E., & Schwartz, R. W. (2006). A Maxwell Garnett model for dielectric mixtures containing conducting particles at optical frequencies. *Progress In Electromagnetics Research, 63*, 223-242. doi:10.2528/pier06052601

Li, Z., Rahtu, A., & Gordon, R. G. (2006). Atomic layer deposition of ultrathin copper metal films from a liquid copper(i) amidinate precursor. *Journal of The Electrochemical Society, 153*(11). doi:10.1149/1.2338632

Lozovski, V., & Razumova, M. (2015). Influence of inclusion shape on light absorption in thin au/teflon nanocomposite films. *Journal of the Optical Society of America B, 33*(1), 8. doi:10.1364/josab.33.000008

Maya, L. (1995). Gold nanocomposites. *Journal of Vacuum Science & Technology B: Microelectronics and Nanometer Structures, 13*(2), 361. doi:10.1116/1.587946

Meyer, B. K., Polity, A., Reppin, D., Becker, M., Hering, P., Klar, P. J., . . . Ronning, C. (2012). Binary copper oxide semiconductors: From materials towards devices. *Physica Status Solidi (b), 249*(8), 1487-1509. doi:10.1002/pssb.201248128

Parshina, L., Novodvorsky, O., Khramova, O., Gusev, D., Polyakov, A., Mikhalevsky, V., & Cherebilo, E. (2021). Laser synthesis of non-volatile memristor structures based on tantalum oxide thin films. *Chaos, Solitons & Fractals, 142*, 110460. doi:10.1016/j.chaos.2020.110460

Parsons, G. N., Elam, J. W., George, S. M., Haukka, S., Jeon, H., (Erwin) Kessels, W. M., . . . Rossnagel, S. M. (2013). History of Atomic Layer Deposition and Its Relationship with the American Vacuum Society. *Journal of*

Vacuum Science & Technology A: Vacuum, Surfaces, and Films, 31(5), 050818. doi:10.1116/1.4816548

Poddubny, A., Iorsh, I., Belov, P., & Kivshar, Y. (2013). Hyperbolic Metamaterials. *Nature Photonics, 7*(12), 948-957. doi:10.1038/nphoton.2013.243

Ravindran, R., Gangopadhyay, K., Gangopadhyay, S., Mehta, N., & Biswas, N. (2006). Permittivity enhancement of aluminum oxide thin films with the addition of silver nanoparticles. *Applied Physics Letters, 89*(26), 263511. doi:10.1063/1.2425010

Rossnagel, S. (2001). Sputtering and Sputter deposition. *Handbook of Thin Film Deposition Processes and Techniques,* 319-348. doi:10.1016/b978-081551442-8.50013-4

Sands, J. H., Kobayashi, N. P., Giraldo, B., Cheney, B., & Fryauf, D. M. (2020). Optical properties of aluminum oxide-copper dielectric-metal nanocomposite thin films deposited by sputtering atomic layer augmented deposition (salad). *Low-Dimensional Materials and Devices 2020*. doi:10.1117/12.2569753

Segall, B. (1962). Fermi surface and energy bands of copper. *Physical Review, 125*(1), 109-122. doi:10.1103/physrev.125.109

Smith, D. R., & Pendry, J. B. (2006). Homogenization of metamaterials by field averaging (invited paper). *Journal of the Optical Society of America B, 23*(3), 391. doi:10.1364/josab.23.000391